Redox-Induced Changes in the Geometry and Electronic Structure of Di-μ-oxo-Bridged Manganese Dimers

John E. McGrady and Robert Stranger*

Contribution from the Department of Chemistry, The Faculties, The Australian National University, Canberra, ACT 0200, Australia

Received December 19, 1996. Revised Manuscript Received June 2, 1997[⊗]

Abstract: Broken-symmetry approximate density functional theory has been used to investigate the electronic and structural properties of the complex $Mn_2O_2(NH_3)_8^{z+}$ in three distinct oxidation states, $Mn_2^{IV/IV}$ ($z = 4$), $Mn_2^{III/IV}$ ($z = 3$) and $Mn_2^{III/III}$ ($z = 2$). In $Mn_2^{IV/IV}$ the metal-based electrons are almost completely localized on one center or the other, and occupy the single-ion orbitals derived from the t_{2g} subset of the parent octahedron. The additional two electrons in $Mn_2^{III/III}$ enter d_{z^2} orbitals aligned along the Mn−N^{ax} axis, resulting in a significant elongation of these bonds. Both $d_{x^2-y^2}$ and d_{z^2} orbitals transform as a_1 in C_{2v} symmetry, and so electron density can be transferred from the d_{z^2} orbital on one center to the $d_{x^2-y^2}$ orbital on the other. In the symmetric dimers, $Mn_2^{IV/IV}$ and $Mn_2^{III/III}$, the energetic separation of the d_{z^2} and $d_{x^2-y^2}$ orbitals is sufficiently large to prevent significant delocalization of the metal-based electrons along this pathway. In contrast, a combination of low-spin polarization on Mn^{IV} and weak axial ligand field in Mn^{III} combine to bring the two orbitals close together in the mixed-valence dimer, and the unpaired electron is significantly delocalized. The delocalization of the unpaired electron between d_{z^2} and $d_{x^2-y^2}$ accounts for the structural trends within the series: the loss of electron density from the d_{z^2} orbital at the Mn^{III} site of $Mn_2^{III/IV}$ shortens the Mn^{III}−N^{ax} bond relative to that in the symmetric $Mn_2^{III/III}$ system. In contrast, the Mn^{IV} site in the mixed-valence species is almost identical with that in $Mn_2^{IV/IV}$ because the additional electron density enters a Mn−N nonbonding $d_{x^2-y^2}$ orbital. The magnetic properties of the dimers are dominated by the symmetric $J_{xz/xz}$ and $J_{yz/yz}$ pathways, both of which are ideally oriented for efficient superexchange *via* the oxo bridges. Redox-induced changes in the Heisenberg exchange coupling constant are caused by changes in geometry of the Mn_2O_2 core rather than by the generation of new pathways as a consequence of occupation of additional orbitals. The longer Mn−Mn separation and the more acute O−Mn−O angle in $Mn_2^{IV/IV}$ improve the efficiency of the J_{yz}/J_{yz} pathway, leading to larger coupling constants in the more oxidized species. The delocalization of the unpaired electron in $Mn_2^{III/IV}$ along the crossed pathway also provides a possible explanation for the highly anisotropic hyperfine signal observed in the EPR spectrum of the oxygen-evolving complex.

Introduction

Manganese ions play a central role in the function of a variety of metalloenzymes,[1] most notably in the oxygen-evolving complex (OEC) of photosystem II, the catalytic center for the oxidation of water to molecular oxygen. During the process of oxygen evolution, the OEC cycles through five distinct states,[2] S_0−S_4, the transition from S_0 to S_4 corresponding to the accumulation of four oxidizing equivalents which are eventually used to oxidize water and regenerate S_0. Four manganese atoms are known to be present in the OEC,[3] and calcium and chloride ions are also required for activity,[4] but only indirect evidence is available on the relative disposition of these components within the active site. X-ray absorption fine structure (EXAFS) experiments[5] indicate that Mn−Mn separations of approximately 2.7 and 3.3 Å are present, although substitution studies indicate that the longer distance may in fact be due to a Mn−Ca vector.[5f,g] In addition, approximately six light atoms (O or N) surround each Mn ion in the first coordination sphere,[5h] suggesting octahedral coordination. Several different models for the structure of the OEC have been proposed on the basis of these data, ranging from tetrameric Mn_4 clusters to a dimer of dimers model featuring two essentially isolated Mn_2 units.[6]

In an attempt to mimic the properties of the OEC, a wide variety of bi- and polynuclear manganese systems have been synthesized. Binuclear complexes featuring a di-μ-oxo bridge (either in isolation or in conjunction with a bridging μ-carboxylato group) are particularly commonplace, and significantly all exhibit Mn−Mn separations of approximately 2.7 Å,[7] consistent with the EXAFS data. On this basis, it seems likely that the Mn_2O_2 unit is a component of the OEC, and considerable efforts

[⊗] Abstract published in *Advance ACS Abstracts,* August 1, 1997.

(1) For recent reviews see: (a) Riggs-Gelasco, P. J.; Mei, R.; Penner-Hahn, J. E. In *Mechanistic Bioinorganic Chemistry*; Holden Thorp, H.; Pecoraro, V. L., Eds.; American Chemical Society: Washington, DC, 1995; p 219. (b) Brudvig, G. W. ref 1a, 249. (c) Pecoraro, V. L.; Gelasco, A.; Baldwin, M. J. ref 1a, p 265. (d) Pecoraro, V. L. in *Manganese Redox Enzymes*; Pecoraro, V. L., Ed.; VCH Publishers: New York, 1992; p 197.

(2) Kok, B.; Forbush, B.; McGloin, M. *Photochem. Photobiol.* **1970**, *11*, 457.

(3) (a) Sivaraja, M.; Dismukes, G. C. *Biochemistry* **1988**, *27*, 3467. (b) Yocum, C. F.; Yerkes, C. T.; Blankenship, R. E.; Sharp, R. R.; Babcock, G. T. *Proc. Natl. Acad. Sci. U.S.A.* **1981**, *78*, 7507. (c) Chenaie, G. M.; Martin, I. *Biochim. Biophys. Acta* **1970**, *197*, 219. (d) Murata, N.; Miyao, M.; Omata, T.; Matsunami, H.; Kuwabara, T. *Biochim. Biophys. Acta* **1985**, *765*, 363.

(4) (a) Yocum, C. F. *Biochim. Biophys. Acta* **1991**, *1059*, 1. (b) Debus, R. *Biochim. Biophys. Acta* **1992**, *1102*, 269.

(5) (a) George, G. N.; Prince, R. C.; Cramer, S. P. *Science* **1989**, *243*, 789. (b) Penner-Hahn, J. E.; Fronko, R. M.; Pecoraro, V. L.; Yocum, C. F.; Betts, S. D.; Bowlby, N. R. *J. Am. Chem. Soc.* **1990**, *112*, 2549. (c) Yachandra, V. K.; DeRose, V. J.; Latimer, M. J.; Kukerji, I.; Sauer, K.; Klein, M. P. *Science* **1993**, *260*, 675. (d) Strange, R. W.; Hasnain, S. S. *J. Biochem.* **1992**, *285*, 569. (e) Dexheimer, S. L.; Britt, R. D.; Wieghardt, K.; Bossek, U.; Sauer, K.; Klein, M. P. *Biochemistry* **1990**, *29*, 471. (f) Riggs-Gelasco, P. J.; Mei. R.; Ghanotakis, D. F.; Yocum, C. F.; Penner-Hahn, J. E. *J. Am. Chem. Soc.* **1996**, *118*, 2400. (g) Latimer, M. J.; DeRose, V. J.; Mukerji, I.; Yachandra, V. K.; Sauer, K.; Klein, M. P. *Biochemistry* **1995**, *34*, 10898. (h) Andreasson, L.-E. *Biochim. Biophys. Acta* **1989**, *973*, 465.

(6) (a) Brudvig, G. W.; Crabtree, R. H. *Proc. Natl. Acad. Sci. U.S.A.* **1985**, *82*, 6119. (b) Vincent, J. B.; Christou, G. *Inorg. Chim. Acta* **1987**, *136*, L41.

S0002-7863(96)04360-0 CCC: $14.00

Table 1. Structural and Magnetic Data for $Mn_2O_2L_8^{z+}$ Complexes[a]

	L	Mn−Mn	Mn^{III}−O	Mn^{IV}−O	Mn^{III}−N_{ax}	Mn^{IV}−N_{ax}	Mn^{III}−N_{eq}	Mn^{IV}−N_{eq}	O−Mn^{III}−O	O−Mn^{IV}−O	*J*	ref
$Mn_2^{IV/IV}$	bispicen	2.672		1.811		2.007		2.060		85.0	−126	11
	phen	2.748		1.800		2.010		2.076		80.5	−144	12
	6Me-L_1	2.747		1.774						78.5	NA	13
$Mn_2^{III/IV}$	bispicen	2.659	1.833	1.793	2.169	2.092	NA	NA	NA	NA	NA	14
	tren	2.679	1.850	1.774	2.276	2.050	2.113	2.097	82.5	86.8	−146	15
	bpy	2.716	1.855	1.784	2.217	2.022	2.132	2.075	NA	NA	−147, −150	9a, 12, 16
	tmpa	2.643	1.837	1.777	2.233	2.013	2.079	2.053	NA	NA	−159	17
	cyclam[b]	2.741	1.862	1.788	2.349	2.050	2.123	2.113	80.6	84.6	NA	18
	cyclam[c]	2.731	1.821		2.192		2.111		82.8		−118.5	19
	cyclam[d]	2.729	1.820		2.207		2.128		82.9		NA	19
	cyclam[d]	2.739	1.827		2.220		2.121		82.9		NA	19
	phen	2.700	1.814		2.128		2.105		83.8		−134, −148	9a, 12
	L_1	2.693	1.814		2.110		2.093		84.0		NA	13
$Mn_2^{III/III}$	$6Me_2$-bispicen	2.676	1.840		2.427		2.113		86.7		−86	20
	$6Me_2$-tmpa	2.674	1.830		2.370		2.098		86.1		NA	20
	bispyzen	2.686	1.842		2.323		2.123		86.4		NA	20

[a] Bond lengths in Å, angles in deg, and exchange coupling constants, *J*, in cm^{-1} [b] Triflate counterion. [c] Bromide counterion. [d] Dithionate counterion.

have been made to relate the spectroscopic properties of model systems to those of the OEC. Electron paramagnetic resonance (EPR) spectra are particularly revealing, as the S_2 state of the OEC exhibits a distinctive multiline signal[8] not unlike the 16-line signals of model systems with a di-μ-oxo Mn_2 core in the III/IV oxidation state.[9] Similar features (Mn−Mn separation around 2.7 Å, multiline EPR signal) have also been observed in the superoxidized form of manganese catalaze,[10] an enzyme that catalyzes the disproportionation of H_2O_2 to O_2 and H_2O. Thus it appears that the di-μ-oxo-bridged $Mn_2^{III/IV}$ core may play a significant role in several aspects of oxygen metabolism.

Given the prominence of the Mn_2O_2 structural unit, and also the importance of redox processes in these systems, the availability of di-μ-oxo-bridged dimanganese species in three distinct oxidation states, $Mn_2^{III/III}$, $Mn_2^{III/IV}$, and $Mn_2^{IV/IV}$, presents a unique opportunity to study redox-induced changes in geometric and electronic structure. Structural and magnetic data for complexes of the general formula $L_4Mn(\mu\text{-}O_2)MnL_4$, where L is a nitrogen donor ligand, are summarized in Table 1. Where the structures of the mixed valence species are disordered, averaged bond lengths are shown. The structures of the bi- or tetradentate ligands which provide the N donor atoms are summarized in Chart 1. The geometry of the Mn_2O_2 core is remarkably robust to changes in oxidation state, and Mn−Mn separations vary only between 2.643 and 2.748 Å. Although there is considerable overlap between the different oxidation states, and hence general conclusions must be treated with some caution, the more highly oxidized $Mn_2^{IV/IV}$ systems lie toward the upper end of the range, and have more acute O−Mn−O angles than their $Mn_2^{III/III}$ counterparts. Moreover, in the cases where complexes with identical ancillary ligands have been isolated in two distinct oxidation states ($Mn_2^{IV/IV}$ and $Mn_2^{III/IV}$ for phen and bispicen), *r*Mn−Mn is always larger in the more highly oxidized species. Redox-induced structural change is more obvious in the Mn−N^{ax} bonds, which are some 0.3−0.4 Å longer in the $Mn_2^{III/III}$ species. In the absence of disorder, distinct Mn^{III} and Mn^{IV} sites can be identified in the mixed valence systems. The Mn^{III} sites show the characteristic long Mn−N^{ax} bonds, but the degree of elongation in the mixed valence species is significantly less than that in the symmetric $Mn_2^{III/III}$ systems. The available structural data therefore suggest that the unpaired electron in the mixed valence systems may be partially delocalized.

Magnetic measurements on the model systems indicate that the two manganese ions are antiferromagnetically coupled in each oxidation state, giving rise to $S = 0$, $^1/_2$, and 0 ground states in the $Mn_2^{IV/IV}$, $Mn_2^{III/IV}$, and $Mn_2^{III/III}$ species, respectively. As was the case for the structural data, exchange coupling constants for $Mn_2^{IV/IV}$ and $Mn_2^{III/IV}$ oxidation states are sensitive to the identity of the ancillary ligands, and hence the ranges for the $Mn_2^{III/IV}$ and $Mn_2^{IV/IV}$ systems overlap. Nevertheless, the antiferromagnetic coupling for the more highly oxidized states appear to be significantly larger than that for $Mn_2^{III/III}$.

In this paper we present a detailed analysis of the electronic structure of a model di-μ-oxo-bridged dimer, $Mn_2O_2(NH_3)_8^{z+}$ (Chart 2), in three distinct oxidation states using approximate density functional theory (DFT).[21] Particular emphasis is placed

(7) (a) Holden Thorp, H.; Brudvig, G. W. *New J. Chem.* **1991**, *15*, 479. (b) Wieghardt, K. *Angew. Chem., Int. Ed. Engl.* **1989**, *28*, 1153.
(8) (a) Dismukes, G. C.; Siderer, Y. *Proc. Natl. Acad. Sci. USA* **1981**, *78*, 274. (b) Hansson, Ö.; Andreasson, L.-E. *Biochim. Biophys. Acta* **1982**, *670*, 261. (c) Brudvig, G. W.; Crabtree, R. H. *Proc. Natl. Acad. Sci., U.S.A.* **1986**, *83*, 4586. (d) Brudvig, G. W. *Advanced EPR: Applications in Biology and Biochemistry*; Hoff, A. J., Ed.; Elsevier: Amsterdam, 1989; p 839. (e) Rutherford, A. W.; Boussac, A.; Zimmermann, J.-L. *New J. Chem.* **1991**, *15*, 491.
(9) (a) Cooper, S. R.; Dismukes, G. C.; Klein, M. P.; Calvin, M. *J. Am. Chem. Soc.* **1978**, *100*, 7248. (b) Cooper, S. R.; Calvin, M. *J. Am. Chem. Soc.* **1977**, *99*, 6623.
(10) (a) Waldo, G. S.; Yu, S.; Penner-Hahn, J. E. *J. Am. Chem. Soc.* **1992**, *114*, 5869. (b) Fronko, R. M.; Penner-Hahn, J. E.; Bender, C. J. *J. Am. Chem. Soc.* **1989**, *111*, 3221. (c) Khangulov, S. V.; Barynin, V. V.; Antonyuk-Barynina, S. V. *Biochim. Biophys. Acta* **1990**, *1020*, 25.
(11) Goodson, P. A.; Glerup, J.; Hodgson, D. J.; Michelsen, K.; Pedersen, E. *Inorg. Chem.* **1990**, *29*, 503.
(12) Stebler, M.; Ludi, A.; Bürgi, H.-B. *Inorg. Chem.* **1986**, *25*, 4743.
(13) Oki, A. R.; Glerup, J.; Hodgson, D. J. *Inorg. Chem.* **1990**, *29*, 2435.
(14) Collins, M. A.; Hodgson, D. J.; Michelsen, K.; Towle, D. K. *J. Chem. Soc., Chem. Commun.* **1987**, 1659.
(15) Hagen, K. S.; Armstrong, W. H.; Hope, H. *Inorg. Chem.* **1988**, *27*, 969.
(16) Plaksin, P. M.; Stoufer, R. C.; Mathew, M.; Palenik, G. J. *J. Am. Chem. Soc.* **1972**, *94*, 2121.
(17) (a) Suzuki, M.; Tokura, S.; Sihara, M.; Uehara, A. *Chem. Lett.* **1988**, 477. (b) Towle, D. K.; Botsford, C. A.; Hodgson, D. J. *Inorg. Chim. Acta* **1988**, *141*, 167.
(18) Brewer, K. J.; Calvin, M.; Lumpkin, R. S.; Otvos, J. W.; Spreer, L. O. *Inorg. Chem.* **1989**, *28*, 4446.
(19) Goodson, P. A.; Glerup, J.; Hodgson, D. J.; Michelsen, K. *Inorg. Chim. Acta* **1990**, *172*, 49.
(20) Goodson, P. A.; Oki, A. R.; Glerup, J.; Hodgson, D. J. *J. Am. Chem. Soc.* **1990**, *112*, 6248.

Chart 1. Structures of Nitrogen-Donor Ligands Described in Table 1

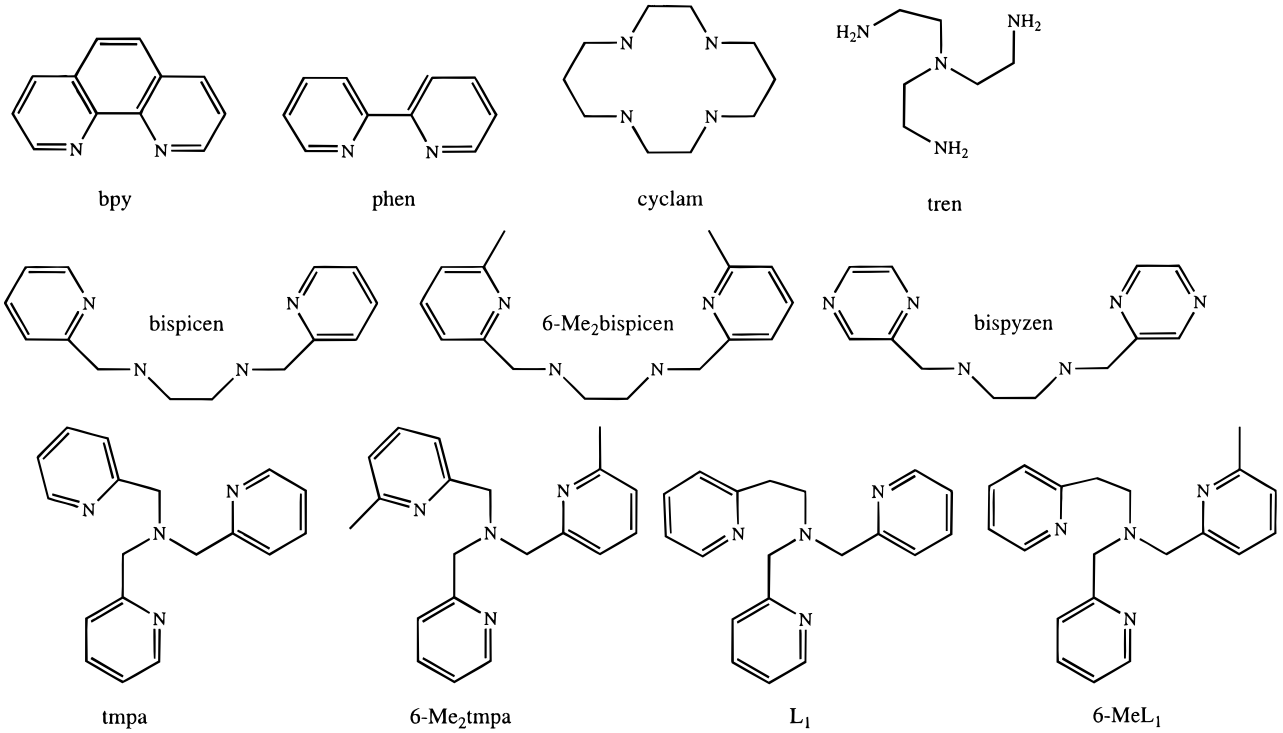

Chart 2. Symmetry Properties of the Metal- and Oxo-Based Orbitals in the $Mn_2O_2(NH_3)_8$ Model System

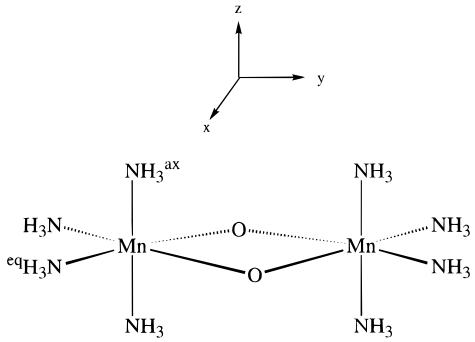

Mn	s	a_1	O	p_z	$a_2 + b_2$
	p	a_1, b_1, b_2		p_x	$a_1 + b_1$
	d_{z^2}	a_1		p_y	$a_1 + b_1$
	$d_{x^2-y^2}$	a_1			
	d_{xz}	a_2			
	d_{yz}	b_2			
	d_{xy}	b_1			

on the electronic and structural changes induced by successive reduction of the $Mn_2^{IV/IV}$ core ($z = 4$) through the mixed-valence $Mn_2^{III/IV}$ form ($z = 3$) to $Mn_2^{III/III}$ ($z = 2$). The model system clearly neglects the steric constraints of the hydrocarbon backbones on the ancillary ligands, and also the electronic differences between aliphatic and aromatic nitrogen. While this precludes comparison of the calculated results with any one individual complex, the structural and magnetic data summarized in Table 1 suggest that the precise nature of the ligand does not exert a dominant influence on either the structural or magnetic properties of the systems. Furthermore, the model system has the advantage of allowing the analysis of the redox-induced electronic and structural changes within a constant ligand environment, a comparison that is not possible within the body of available experimental data.

Approximate density functional theory (DFT) has been used with great success in recent years to provide an accurate description of the electronic structure of a variety of metal-containing complexes.[21] Antiferromagnetically coupled systems, where the metal-based electrons are not completely delocalized, provide a particularly stringent test of the methodology, as the energetic separations between different spin states are relatively small. The broken-symmetry technique developed by Noodleman *et al.*[22] represents a major advance in the treatment of such systems, because by removing all symmetry elements connecting the two metal centers in a dimer, spin α and spin β electrons are permitted to localize on opposite sides of the molecule. It is important to note, however, that breaking the symmetry does not force the electrons to localize, and therefore a delocalized solution can still arise if this state lies lower than the corresponding localized one. Thus the broken-symmetry methodology embraces weak, intermediate, and strong metal−metal interactions, and therefore provides a highly flexible technique for studying periodic and redox-induced trends in electronic structure. The method has now been applied to a variety of transition metal dimers and larger clusters, and in general gives an accurate description of antiferromagnetic coupling between metal ions.[23] We have also recently reported the importance of breaking the symmetry when calculating geometries of systems featuring weakly coupled electrons.[24] The focus of this paper is to calculate optimized structures for di-μ-oxo-bridged complexes in three distinct oxidation states. Given the substantial structural and magnetic

(21) Ziegler, T. *Chem Rev.* **1991**, *91*, 651.

(22) Noodleman, L. *J. Chem. Phys.* **1981**, *74*, 5737.

(23) (a) Medley, G. A.; Stranger, R. *Inorg. Chem.* **1994**, *33*, 3976. (b) Mouesca, J.-M.; Chen, J. L.; Noodleman, L.; Bashford, D.; Case, D. A. *J. Am. Chem. Soc.* **1994**, *116*, 11898. (c) Jacobsen, H.; Kraatz, H. B.; Ziegler, T.; Boorman, P. M. *J. Am. Chem. Soc.* **1992**, *114*, 7851. (d) Ross, P. K.; Solomon, E. I. *J. Am. Chem. Soc.* **1991**, *113*, 3246. (e) Bencini, A.; Gatteschi, D. *J. Am. Chem. Soc.* **1986**, *108*, 5763. (f) Aizman, A.; Case, D. A. *J. Am. Chem. Soc.* **1982**, *104*, 3269.

(24) (a) Lovell, T.; McGrady, J. E.; Stranger, R.; Macgregor, S. A. *Inorg. Chem.* **1996**, *35*, 3079. (b) MacGregor, S. A.; Stranger, R.; Lovell, T.; McGrady, J. E.; Heath, G. A. *J. Chem. Soc., Dalton Trans.* **1996**, 4485. (c) McGrady, J. E.; Stranger, R.; Lovell, T. *J. Phys. Chem.* In press.

evidence for electron localization in the manganese systems (see Table 1), we feel that the broken-symmetry methodology will be essential for an accurate description of systems containing the Mn_2O_2 core. Accordingly, the full D_{2h} symmetry of the model system is reduced to C_{2v} by removing all elements connecting the two manganese centers. The molecular coordinate axis is chosen so that the local z axis at each metal atom is perpendicular to the plane defined by the Mn_2O_2 core, and therefore directed approximately along the $Mn-N^{ax}$ vector. The symmetry properties of the metal- and oxo-based orbitals in this coordinate system are also summarized in Chart 2.

Only a limited number of theoretical studies into the structure and function of biologically relevant manganese dimers have been performed, probably because of the relatively recent appreciation of their significance. Potential mechanisms for oxygen evolution from various model manganese clusters, including di-μ-oxo-bridged dimers, have been investigated with use of the extended Hückel theory,[25] and the qualitative features of these calculations were used to interpret the optical spectra of mixed-valence systems.[26] Very recently, Noodleman and co-workers presented a detailed analysis of the electronic structure and magnetic properties of a variety of di-μ-oxo, μ-peroxo and di-μ-oxo, μ-carboxylato bridged manganese dimers using broken-symmetry density functional theory.[27] Related iron species have received more attention because of their relevance to the properties of metalloenzymes such as hemerythrin, methane monooxygenase, and ribonucleotide reductase. Solomon and co-workers have reported a detailed study of the electronic structure and spectroscopic properties of μ-oxo and μ-oxo, di-μ-carboxylato diiron systems using broken-symmetry SCF-Xα-SW calculations.[28] In both model systems, the broken-symmetry state was formulated as containing antiferromagnetically coupled high-spin d^5 Fe^{III} ions, with almost complete localization of the metal-based electrons. A spin-restricted density functional study of a di-μ-oxo-bridged species containing the Fe_2O_2 core has also been reported by Ghosh *et al.*[29] However, in their investigation, the two Fe centers were related by symmetry and hence a localized description of the electronic structure was precluded. Given the relatively short Fe−Fe separation in this case, it is possible the reported delocalized wave function featuring low-spin Fe^{III} ions may represent the true ground state, but it is important to emphasize that this description was an inevitable consequence of the chosen computational technique.

Computational Details

All approximate density functional calculations reported in this work were performed with the Amsterdam Density Functional (ADF) program version 2.0.1.[30] A double-ζ Slater-type orbital basis set[31] extended with a single polarization function was used to describe hydrogen, nitrogen, and oxygen, while the manganese atoms were modeled with a triple-ζ basis set. Electrons in orbitals up to and including 1s {N,O} and 3p {Mn} were considered to be part of the core and treated in accordance with the frozen-core approximation. All calculations were performed in an unrestricted manner with use of C_{2v} symmetry. The LDA approximation was used,[32] along with the local exchange-correlation potential of Vosko, Wilk, and Nusair.[33] Gradient corrections to exchange (Becke)[34] and correlation (Perdew)[35] were also incorporated. The geometries of all broken-symmetry and high-spin states were optimized by using the gradient algorithm of Versluis and Ziegler,[36] with the restriction that all N−H bonds remained at 1.01 Å and all H−N−H angles at 109.5°.

Table 2. Optimized Structural Parameters for $Mn_2^{IV/IV}$, $Mn_2^{III/IV}$, and $Mn_2^{III/III}$

	$Mn_2^{IV/IV}$	$Mn_2^{III/IV}$	$Mn_2^{III/III}$
Mn−Mn/Å	2.866	2.783	2.716
$Mn^{IV}-O$/Å	1.842	1.800	
$Mn^{IV}-N^{ax}$/Å	2.137	2.117	
$Mn^{IV}-N^{eq}$/Å	2.215	2.227	
$O-Mn^{IV}-O$/deg	77.9	85.2	
$Mn^{III}-O$/Å		1.873	1.840
$Mn^{III}-N^{ax}$/Å		2.459	2.504
$Mn^{III}-N^{eq}$/Å		2.210	2.231
$O-Mn^{III}-O$/deg		79.5	84.8

Results and Discussion

Optimized structural parameters for the broken-symmetry states of $Mn_2O_2(NH_3)_8^{4+}$ ($Mn_2^{IV/IV}$), $Mn_2O_2(NH_3)_8^{3+}$ ($Mn_2^{III/IV}$), and $Mn_2O_2(NH_3)_8^{2+}$ ($Mn_2^{III/III}$) are summarized in Table 2. The energies and compositions of the metal-based orbitals, along with the highest occupied ligand-based orbital ($11b_1$ in each case), are summarized in Tables 3−5. The relative energies and extent of localization (defined as percent Mn^l − percent Mn^r) of the metal-based orbitals of each system are illustrated in Figure 1. Mulliken population analyses of the charge distributions for each oxidation state are summarized in Table 6.

$Mn_2^{IV/IV}$. The calculated structural features of the Mn_2O_2 core are in generally good agreement with the crystallographic data shown in Table 1. The Mn−Mn separation of 2.866 Å is approximately 0.1 Å longer than the longest experimental value, but the O−Mn−O angle of 77.9° is consistent with the acute angles observed in complexes in the highest oxidation state. Although the use of NH_3 ligands in the model systems precludes comparison with any individual complex, the calculated Mn−N bond lengths also mirror experimental trends, with the $Mn-N^{eq}$ bonds approximately 0.08 Å longer than their $Mn-N^{ax}$ counterparts as a consequence of the strong *trans* influence of the oxo ligands.

The basic features of the electronic structure of $Mn_2^{IV/IV}$ (Table 3, Figure 1a) can be most easily interpreted in terms of two isolated Mn^{IV} ions. The lowest lying metal-based orbitals ($16a_1$, $6a_2$ and $10b_2$) are related to the t_{2g} orbitals $d_{x^2-y^2}$, d_{xz}, and d_{yz} of the parent octahedron, and the three d electrons on each Mn^{IV} ion are sufficient to singly occupy each of these orbitals. On the left-hand side, the three spin α orbitals are occupied, whereas on the right-hand side the electrons enter the spin β orbitals, resulting in a spin singlet ground state. These majority-spin orbitals on each center are stabilized by spin polarization relative to their minority-spin counterparts ($17a_1$, $7a_2$, and $11b_2$), and the t_{2g} band is split by approximately 2.5 eV. While this splitting is substantial, it is not sufficient to displace the majority-spin t_{2g} orbitals below the highest occupied ligand-based orbitals, as has been observed in other systems

(25) Prosperio, D. M.; Hoffmann, R.; Dismukes, G. C. *J. Am. Chem. Soc*. **1992**, *114*, 4374.
(26) Gamelin, D. R.; Kirk, M. L.; Stemmler, T. L.; Pal, S.; Armstrong, W. H.; Penner- Hahn, J. E.; Solomon, E. I. *J. Am. Chem. Soc*. **1994**, *116*, 2392.
(27) Zhao, X. G.; Richardson, W. H.; Chen, J.-L.; Li, J.; Noodleman, L.; Tsai, H.-L.; Hendrickson, D. N. *Inorg. Chem*. **1997**, *36*, 1198.
(28) Brown, C. A.; Remar, G. J.; Musselman, R. L.; Solomon, E. I. *Inorg. Chem*. **1995**, *34*, 688.
(29) Ghosh, A.; Almlöf, J.; Que, L. *Angew. Chem., Int. Ed. Engl.* **1996**, *35*, 770.
(30) (a) Baerends, E. J.; Ellis, D. E.; Ros, P. *Chem. Phys.* **1973**, *2*, 42. (b) Baerends, E. J.; Ros, P. *Int. J. Quantum Chem.* **1978**, *S12*, 169.
(31) Vernooijs, P.; Snijders, G. L.; Baerends, E. J. *Slater Type Basis Functions for the Whole Periodic Table*; Internal Report, Vrije Universiteit: Amsterdam, 1981.
(32) Parr, R. G.; Yang, W. *Density Functional Theory of Atoms and Molecules*, Oxford University Press: New York, 1989.
(33) Vosko, S. H.; Wilk, L.; Nusair, M. *Can. J. Phys.* **1980**, *58*, 1200.
(34) Becke, A. D. *J. Chem. Phys.* **1986**, *84*, 4524.
(35) Perdew, J. P. *Phys. Rev. B* **1986**, *33*, 8822.
(36) Versluis, L.; Ziegler, T. *J. Chem. Phys.* **1988**, *88*, 322.

Table 3. Energies and Compositions of the Molecular Orbitals of $Mn_2O_2(NH_3)_8^{4+}$

		left				right		
	energy/eV	$^{eq}NH_3$	$^{ax}NH_3$	Mn	O_{br}	Mn	$^{ax}NH_3$	$^{eq}NH_3$
$13b_1\downarrow$	−17.585	11	0	62(d_{xy})	22	3	1	1
$13b_1\uparrow$	−17.585	0	0	2	20	63(d_{xy})	0	13
$19a_1\downarrow$	−18.236	6	21	65(d_{z^2})	6	1($d_{x^2-y^2}$)	0	1
$19a_1\uparrow$	−18.236	1	0	1($d_{x^2-y^2}$)	6	65(d_{z^2})	21	6
$12b_1\downarrow$	−18.695	0	0	4	33	50(d_{xy})	0	13
$12b_1\uparrow$	−18.695	13	0	50(d_{xy})	33	4	0	0
$18a_1\downarrow$	−18.966	2	0	22($d_{x^2-y^2}$)	14	46(d_{z^2})	13	3
$18a_1\uparrow$	−18.966	1	13	46(d_{z^2})	14	22($d_{x^2-y^2}$)	0	2
$11b_2\downarrow$	−19.335	0	3	76(d_{yz})	18	2	1	0
$11b_2\uparrow$	−19.335	0	1	2	18	76(d_{yz})	3	0
$7a_2\downarrow$	−19.536	0	1	80(d_{xz})	18	1	0	0
$7a_2\uparrow$	−19.536	0	0	1	18	80(d_{xz})	1	0
$17a_1\downarrow$	−19.759	1	0	45($d_{x^2-y^2}$)	2	30(d_{z^2})	15	7
$17a_1\uparrow$	−19.759	15	7	30(d_{z^2})	2	45($d_{x^2-y^2}$)	0	1
$10b_2\downarrow$	−21.796	1	2	15	27	43(d_{yz})	12	0
$10b_2\uparrow$	−21.796	0	12	43(d_{yz})	27	15	2	1
$6a_2\downarrow$	−21.991	0	1	15	48	35(d_{xz})	1	0
$6a_2\uparrow$	−21.991	0	1	35(d_{xz})	48	15	1	0
$16a_1\downarrow$	−22.168	6	2	5(d_{z^2})	25	60($d_{x^2-y^2}$)	0	2
$16a_1\uparrow$	−22.168	2	0	60($d_{x^2-y^2}$)	25	5(d_{z^2})	2	6
$11b_1\downarrow$	−22.005	24	1	3	56	2	0	14
$11b_1\uparrow$	−22.005	14	0	2	56	3	1	24

Table 4. Energies and Compositions of the Molecular Orbitals of $Mn_2O_2(NH_3)_8^{2+}$

		left				right		
	energy/eV	$^{eq}NH_3$	$^{ax}NH_3$	Mn	O_{br}	Mn	$^{ax}NH_3$	$^{eq}NH_3$
$13b_1\downarrow$	−7.506	7	0	70(d_{xy})	19	1	2	1
$13b_1\uparrow$	−7.506	1	2	1	19	70(d_{xy})	0	7
$19a_1\downarrow$	−8.191	1	13	83(d_{z^2})	3	0	0	0
$19a_1\uparrow$	−8.191	0	0	0	3	83(d_{z^2})	13	1
$11b_2\downarrow$	−8.849	1	2	86(d_{yz})	10	1	0	0
$11b_2\uparrow$	−8.849	0	0	1	10	86(d_{yz})	2	1
$7a_2\downarrow$	−8.857	1	0	84(d_{xz})	13	2	0	0
$7a_2\uparrow$	−8.857	0	0	2	13	84(d_{xz})	0	1
$18a_1\downarrow$	−8.964	0	2	84($d_{x^2-y^2}$)	11	3(d_{z^2})	0	0
$18a_1\uparrow$	−8.964	0	0	3(d_{z^2})	11	84($d_{x^2-y^2}$)	2	0
$12b_1\downarrow$	−9.075	0	0	1	34	54(d_{xy})	1	10
$12b_1\uparrow$	−9.075	10	1	54(d_{xy})	34	1	0	0
$17a_1\downarrow$	−11.094	1	0	5($d_{x^2-y^2}$)	5	61(d_{z^2})	22	3
$17a_1\uparrow$	−11.094	3	22	61(d_{z^2})	5	5($d_{x^2-y^2}$)	0	1
$10b_2\downarrow$	−11.797	1	1	7	30	54(d_{yz})	7	0
$10b_2\uparrow$	−11.797	0	7	54(d_{yz})	30	7	1	1
$6a_2\downarrow$	−11.871	0	0	11	39	49(d_{xz})	0	1
$6a_2\uparrow$	−11.871	1	0	49(d_{xz})	39	11	0	0
$16a_1\downarrow$	−12.143	2	0	4(d_{z^2})	31	62($d_{x^2-y^2}$)	0	1
$16a_1\uparrow$	−12.143	0	0	62($d_{x^2-y^2}$)	31	4(d_{z^2})	0	2
$11b_1\downarrow$	−13.183	8	0	4	65	6	1	16
$11b_1\uparrow$	−13.183	16	1	6	65	4	0	8

with less electronegative ligands.[37] Some 3.2 eV above the majority-spin t_{2g} orbitals lie the majority-spin e_g subset, $18a_1$ and $12b_1$. Their minority-spin counterparts, $19a_1$ and $13b_1$, lie a further 0.8 eV higher in energy, the smaller spin polarization splitting of the e_g set being related to the lower metal character in the these orbitals.

Having interpreted the general features of the molecular orbital diagram on the basis of non-interacting, approximately octahedral Mn^{IV} ions, we now consider in more detail the subtle effects of the low-symmetry ligand field and the metal−metal interaction. Contour plots for the spin α orbitals of $Mn_2^{IV/IV}$ are shown in Figure 2 (throughout the discussion of the symmetric $Mn_2^{IV/IV}$ and $Mn_2^{III/III}$ species attention is focussed on the spin α orbitals—their spin β counterparts are simply related to those shown in Figure 2 by reflection in the plane normal to the Mn−Mn axis containing the two oxo ligands). The reduction in local symmetry from O_h to C_{2v} removes the degeneracy of both the t_{2g} and e_g orbitals, and the e_g pair in particular is strongly split. The contour plots in Figure 2 indicate that the $12b_1\uparrow$ and $13b_1\uparrow$ orbitals are strongly antibonding with respect to the oxo ligands, whereas the $18a_1\uparrow$ and $19a_1\uparrow$ orbitals interact primarily with the less electron donating axial NH_3 ligands, and are consequently less destabilized than their b_1 counterparts. The low-symmetry ligand environment has a smaller influence on the essentially nonbonding t_{2g} subset, but as these orbitals are occupied and hence determine the magnetic properties of the system, a detailed discussion of their composition is merited.

The metal−metal interaction may be broken down into separate contributions from the different symmetry representations. In the limit of strong metal−metal bonding, the $d_{x^2-y^2}$ orbitals (a_1 symmetry) overlap to give Mn−Mn σ and σ^*

(37) Noodleman, L.; Norman, J. G., Jr.; Osborne, J. H.; Aizman, A.; Case, D. A. *J. Am. Chem. Soc.* **1985**, *107*, 3418.

Table 5. Energies and Compositions of the Molecular Orbitals of $Mn_2O_2(NH_3)_8^{3+}$

		left				right		
	energy/eV	$^{eq}NH_3$	$^{ax}NH_3$	Mn	O_{br}	Mn	$^{ax}NH_3$	$^{eq}NH_3$
$13b_1\downarrow$	−12.541	9	0	70(d_{xy})	18	1	1	1
$13b_1\uparrow$	−12.683	0	0	1	24	65(d_{xy})	0	10
$19a_1\downarrow$	−13.014	2	13	77(d_{z^2})	3	1	0	0
$19a_1\uparrow$	−13.483	0	0	1	8	67(d_{z^2})	18	6
$12b_1\downarrow$	−13.672	0	0	2	32	55(d_{xy})	0	11
$18a_1\downarrow$	−13.782	0	1	68($d_{x^2-y^2}$)	13	12(d_{z^2})	6	0
$11b_2\downarrow$	−13.799	0	2	87(d_{xz})	10	1	0	0
$7a_2\downarrow$	−13.923	0	0	89(d_{yz})	9	1	1	0
$12b_1\uparrow$	−14.083	13	0	51(d_{xy})	33	2	0	1
$18a_1\uparrow$	−14.401	0	3	6(d_{z^2})	16	75($d_{x^2-y^2}$)	0	0
$11b_2\uparrow$	−14.634	0	1	3	20	74(d_{xz})	2	0
$7a_2\uparrow$	−14.655	0	0	2	23	75(d_{yz})	0	0
$17a_1\downarrow$	−14.788	1	0	23($d_{x^2-y^2}$)	3	47(d_{z^2})	17	5
$17a_1\uparrow$	−15.736	7	31	48(d_{z^2})	2	12($d_{x^2-y^2}$)	0	0
$10b_2\uparrow$	−16.825	14	0	48(d_{yz})	21	15	2	0
$10b_2\downarrow$	−16.949	1	3	7	34	48(d_{yz})	7	0
$16a_1\downarrow$	−16.955	3	0	4(d_{z^2})	28	64($d_{x^2-y^2}$)	0	1
$6a_2\downarrow$	−17.035	1	0	8	45	46(d_{xz})	0	0
$6a_2\uparrow$	−17.096	0	0	46(d_{xz})	34	20	0	0
$16a_1\uparrow$	−17.386	0	5	57($d_{x^2-y^2}$)	20	14(d_{z^2})	0	0
$11b_1\uparrow$	−17.635	21	0	4	56	3	0	13
$11b_1\downarrow$	−17.760	14	0	2	59	2	1	22

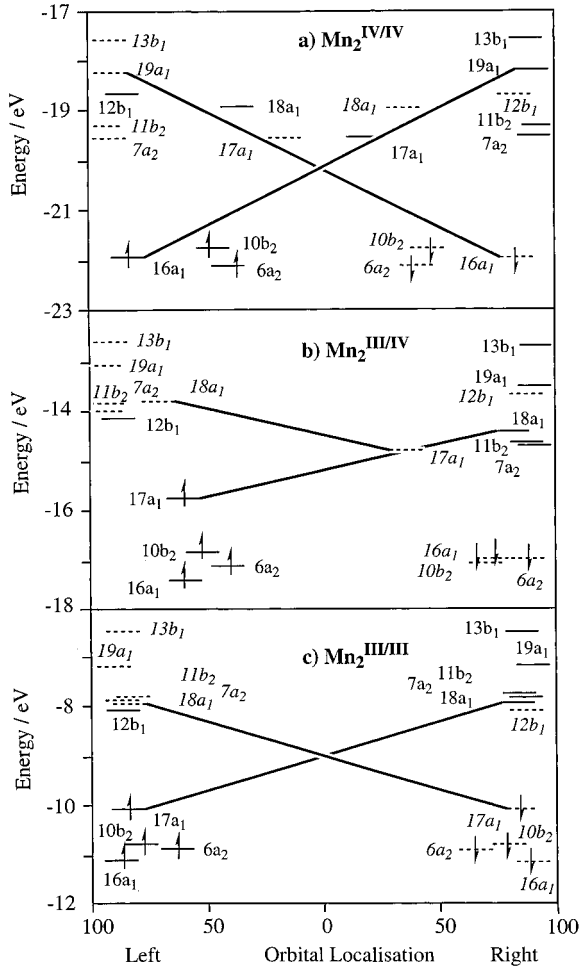

Figure 1. Energies and percent localization of the metal-based orbitals of $Mn_2^{IV/IV}$, $Mn_2^{III/IV}$, and $Mn_2^{III/III}$. Orbitals involved in the cross-exchange pathway are linked by bold lines.

molecular orbitals, whereas d_{yz} (b_2) and d_{xz} (a_2) give π/π^* and δ/δ^* pairs, respectively. However, the contour plots in Figure 2 indicate that direct overlap of metal-based orbitals is negligible in each case, and so the metal−metal interaction will instead be dominated by superexchange pathways *via* the bridging ligands. Three symmetric superexchange pathways, denoted $J_{x^2-y^2/x^2-y^2}$, $J_{xz/xz}$, and $J_{yz/yz}$ are summarized in Chart 3. It is apparent from the scheme that the out-of-plane oxo p orbitals (p_z) overlap with d_{xz} and d_{yz} orbitals on both centers, and hence $J_{xz/xz}$ and $J_{yz/yz}$ form efficient superexchange pathways. In contrast, if the in-plane p orbitals ($p_{x,y}$) on the oxo ligands are aligned for optimal overlap with the $d_{x^2-y^2}$ orbital on one metal center, they lie approximately orthogonal to the corresponding orbital on the opposite center. Superexchange *via* the $J_{x^2-y^2/x^2-y^2}$ pathway is therefore likely to be less efficient. While the alignment of the in-plane oxo p orbitals for optimal overlap with one $d_{x^2-y^2}$ orbital is incompatible with efficient overlap with $d_{x^2-y^2}$ on the other, it does allow for significant overlap with the torus of a d_{z^2} orbital, which also transforms as a_1, on the opposite center ($J_{x^2-y^2/z^2}$, Chart 3). Thus within a_1 symmetry there are two possible exchange pathways, one symmetric ($J_{x^2-y^2/x^2-y^2}$) and the other "crossed" ($J_{x^2-y^2/z^2}$). On a qualitative basis, we anticipate that the latter will be most important.

The fundamental difference between the $J_{xz/xz}$ and $J_{yz/yz}$ pathways on one hand and $J_{x^2-y^2/x^2-y^2}$ on the other is reflected in compositions of the $6a_2\uparrow$, $10b_2\uparrow$, and $16a_1\uparrow$ orbitals. While $6a_2\uparrow$ and $10b_2\uparrow$ are significantly delocalized over both centers (Mn^l:Mn^r = 35:15 and 43:15, respectively), the $16a_1\uparrow$ orbital remains essentially localized (60:5) on one side of the molecule. Furthermore, the contour plot of $16a_1\uparrow$ shown in Figure 2 illustrates that the 5% Mn^r character is in fact d_{z^2}, confirming that the crossed exchange pathway, $J_{x^2-y^2/z^2}$, dominates its symmetric $J_{x^2-y^2/x^2-y^2}$ counterpart. Given the favorable orientation of $d_{x^2-y^2}$, d_{z^2}, and in-plane p orbitals for superexchange, it is perhaps surprising that the delocalization in $16a_1\uparrow$ is not more significant. However, the occupied spin α $d_{x^2-y^2}$ orbital on Mn^l (primarily found in $16a_1\uparrow$) is of majority spin, and hence stabilized by spin polarization, whereas the vacant spin α d_{z^2} orbital on Mn^r ($19a_1\uparrow$) is of minority spin, and so destabilized. Both spin polarization and ligand-field splittings therefore serve to increase the energetic separation between the two interacting orbitals, and the resultant splitting of almost 4 eV is sufficiently large to ensure that both $16a_1\uparrow$ and $19a_1\uparrow$ remain almost completely localized. In contrast, the vacant $17a_1\uparrow$ and $18a_1\uparrow$ orbitals are significantly delocalized, with Mn^l:Mn^r ratios of 30:45 and 46:22, respectively. In this case, the $d_{x^2-y^2}$ orbital on

Table 6. Mulliken Population Analyses for $Mn_2^{IV/IV}$, $Mn_2^{III/IV}$, and $Mn_2^{IV/IV}$

	$Mn_2^{III/III}$				$Mn_2^{III/IV}$				$Mn_2^{IV/IV}$			
	Mn^{III}		Mn^{III}		Mn^{III}		Mn^{IV}		Mn^{IV}		Mn^{IV}	
	↑	↓	↑	↓	↑	↓	↑	↓	↑	↓	↑	↓
s (a_1)	0.24	0.18	0.18	0.24	0.23	0.18	0.18	0.21	0.21	0.18	0.18	0.21
p (a_1,b_1,b_2)	0.21	0.13	0.13	0.21	0.22	0.15	0.14	0.19	0.21	0.15	0.15	0.21
d_{xy} (b_1)	0.47	0.29	0.29	0.47	0.50	0.30	0.36	0.47	0.51	0.37	0.37	0.51
d_{z^2} (a_1)	0.99	0.17	0.17	0.99	0.95	0.21	0.34	0.43	0.49	0.35	0.35	0.49
$d_{x^2-y^2}$ (a_1)	1.00	0.15	0.15	1.00	1.00	0.09	0.25	0.99	0.99	0.13	0.13	0.99
d_{xz} (a_2)	0.99	0.15	0.15	0.99	0.99	0.11	0.25	0.99	0.99	0.20	0.20	0.99
d_{yz} (b_2)	1.00	0.14	0.14	1.00	0.99	0.13	0.26	1.00	0.99	0.24	0.24	0.99
spin pop (↑−↓)	3.69		−3.69		3.71		−2.50		2.78		−2.78	

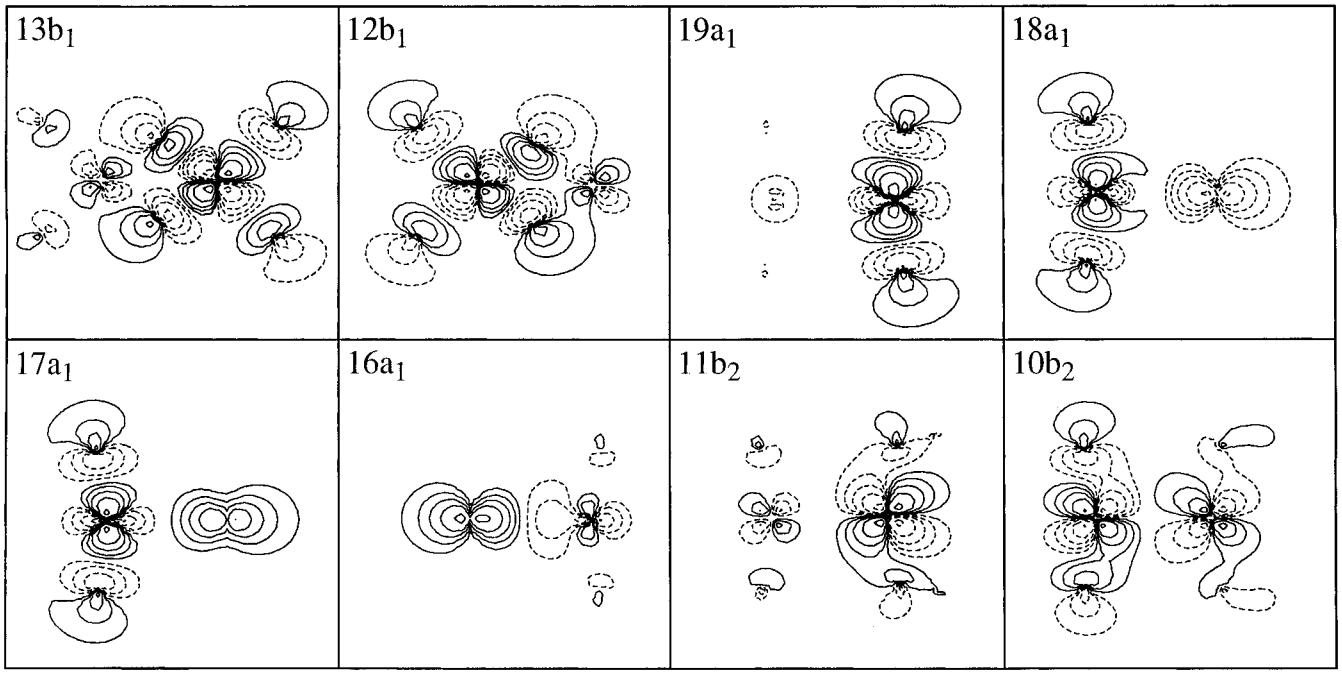

Figure 2. Contour plots for the spin α metal-based orbitals of $Mn_2^{IV/IV}$. Orbitals of a_1 and b_2 symmetry are shown in a plane defined by the Mn and N^{ax} atoms, whereas those of b_1 symmetry are shown in the Mn_2O_2 plane. Successive contours correspond to 0.02, 0.05, 0.10, 0.2, and 0.5 $(electrons/au^3)^{1/2}$

Mn^r (localized primarily in $17a_1$↑) is of minority spin, while the d_{z^2} orbital on Mn^l (primarily in $18a_1$↑) is of majority spin. The combined effects of spin polarization and ligand field splitting therefore reduce the energetic separation of the two orbitals, and the resultant gap of only 1.0 eV gives rise to the significant mixing observed in both $17a_1$↑ and $18a_1$↑.

The population analysis given in Table 6 confirms the general picture outlined above. The majority-spin $d_{x^2-y^2}$, d_{xz}, and d_{yz} orbitals are fully occupied, and hence have populations approaching 1.0. In a purely ionic crystal field model, all remaining orbitals would have zero population, resulting in a net spin population of ±3.0 per Mn center. Deviations from this idealized situation therefore reflect covalent interactions between the metal and ligands. The minority-spin t_{2g} orbitals attain populations of approximately 0.2 through mixing with the occupied, primarily ligand-based, manifold. The covalent mixing is even greater in the octahedral e_g orbitals, d_{xy} and d_{z^2}, leading to minority-spin populations approaching 0.4. The population of the majority-spin d_{xy} and d_{z^2} orbitals is even larger (0.50) due to the stabilizing influence of spin polarization, which decreases the separation between majority-spin metal and ligand levels, and further enhancing the covalent mixing. In describing the influence of covalent bonding on the Mulliken populations, we have focussed on the occupations of the minority-spin orbitals. It is important to appreciate that similar trends will occur in the majority-spin orbitals, but the occupation of both the bonding (principally ligand-based) and antibonding (principally metal-based) majority-spin orbitals results in occupations close to 1.0 in each case, thereby masking the subtle trends found in the minority-spin orbitals.

$Mn_2^{III/III}$. Two-electron reduction of $Mn_2^{IV/IV}$ to the $Mn_2^{III/III}$ species causes several significant structural changes. First, the Mn_2O_2 core is compressed along the Mn−Mn axis, resulting in a calculated Mn−Mn separation of 2.716 Å and a larger O−Mn−O angle of 84.8°. Although structural data on $Mn_2^{III/III}$ complexes are limited, both features are consistent with the trends revealed in Table 1. The most striking contrast between the two oxidation states, however, arises not within the Mn_2O_2 core but in the Mn−N bonds. There is a marginal increase in $Mn-N^{eq}$ separation in $Mn_2^{III/III}$, consistent with the lower prevailing oxidation state, but the optimized $Mn-N^{ax}$ bond length increases by over 0.35 Å to 2.504 Å. This elongation is present in all $Mn_2^{III/III}$ complexes shown in Table 1, although the precise length of the $Mn-N^{ax}$ bond is highly dependent on the identity of the ancillary ligand.

The expansion of the axial $Mn-NH_3$ bond has been attributed to a Jahn−Teller-type effect,[19,20] where the additional electron enters a $Mn-N^{ax}$ antibonding (d_{z^2}) orbital, giving a high-spin d^4 Mn^{III} ion. The composition of the orbitals shown in Table 4 confirms that this is indeed the case, and the HOMO ($17a_1$↑) is principally composed of majority-spin d_{z^2} orbitals, with minority-spin $d_{x^2-y^2}$ character found at higher energy in

Chart 3. Exchange Coupling Pathways in the Mn_2O_2 Core

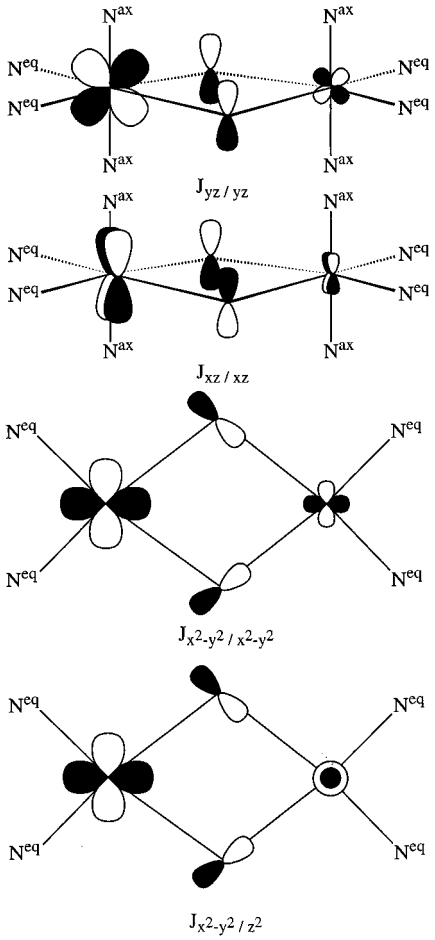

$18a_1\uparrow$. There has therefore been a reversal in ordering relative to $Mn_2^{IV/IV}$, where the majority-spin d_{z^2} orbital (localized in $18a_1\uparrow$) lies above minority-spin $d_{x^2-y^2}$ ($17a_1\uparrow$). This significant reorganization is caused by changes in both spin polarization and effective ligand-field splitting: the spin polarization splitting is increased due to the presence of an additional electron per Mn center in $Mn_2^{III/III}$, while the lengthening of the $Mn-N^{ax}$ bond reduces the ligand field, stabilizing the d_{z^2} orbital. The net result is that the majority-spin d_{z^2} orbitals fall below their minority-spin $d_{x^2-y^2}$ counterparts, and the Mn^{III} ions adopt a high-spin configuration. It is important to emphasize that because both the $d_{x^2-y^2}$ (t_{2g}) and d_{z^2} (e_g) orbitals transform as a_1, the broken symmetry ground state with a metal-based configuration of $(a_1)^2(a_2)^2(b_2)^2(a_1)^2$ is fully compatible with antiferromagnetic coupling of either two high spin $[(t_{2g}\uparrow)^3(e_g\uparrow)^1, S = 2]$ or two low-spin $[(t_{2g}\uparrow)^3(t_{2g}\downarrow)^1, S = 1]$ Mn^{III} centers. The ground state reported above is therefore not enforced by any restrictions imposed in the calculations, but arises simply because, at self-consistency, the state containing the low-spin Mn^{III} ions state lies at higher energy.

The population analysis (Table 6) clearly reflects the change from Mn^{IV} to high spin Mn^{III}. A comparison of the $Mn_2^{IV/IV}$ and $Mn_2^{III/III}$ systems confirms that the additional electron on each metal center has entered a majority-spin d_{z^2} orbital, and in the absence of covalent mixing of metal and ligand orbitals, a net spin population of ±4.0 would arise. The lower minority-spin orbital populations in $Mn_2^{III/III}$ indicate that covalent mixing of metal and ligand orbitals is less significant in the reduced complex, most notably in the d_{z^2} orbital where the population decreases by 0.18. The only exception to this general trend occurs in the minority-spin $d_{x^2-y^2}$ orbital, where the population increases by 0.02 upon reduction. This subtle change is also related to delocalization of electron density along the crossed pathway: in the oxidized $Mn_2^{IV/IV}$ system, there is a net transfer of electron density from the occupied $d_{x^2-y^2}$ orbital to a vacant d_{z^2} orbital on the opposite center, thereby increasing the population of the latter at the expense of the former. After reduction, the d_{z^2} orbital is occupied, driving electron density in the opposite direction ($d_{z^2} \rightarrow d_{x^2-y^2}$). The net result of two-electron reduction is therefore to increase the population of the minority-spin $d_{x^2-y^2}$ orbital as well as majority-spin d_{z^2}.

$Mn_2^{III/IV}$. At first glance, the optimized structure of the $Mn_2^{III/IV}$ dimer is fully consistent with a valence trapped system. The most obvious indication of the presence of distinct Mn^{III} and Mn^{IV} sites is the significantly longer $Mn-N^{ax}$ bond length at the reduced site. The $Mn^{III}-N^{ax}$ bond length (2.459 Å) is however significantly shorter than that in the symmetric $Mn_2^{III/III}$ system (2.504 Å), suggesting that the unpaired electron is not completely localized in the d_{z^2} orbital on the Mn^{III} center.[38] This observation is again completely consistent with the available structural data, where $Mn-N^{ax}$ bond lengths in the mixed-valence dimers (2.169−2.349 Å), are in general shorter than those for the $Mn_2^{III/III}$ complexes (2.323−2.427 Å). In marked contrast, the structural characteristics of the Mn^{IV} site are almost identical with those in $Mn_2^{IV/IV}$, indicating that the residual electron density is not transferred into the d_{z^2} orbital on the opposite Mn^{IV} center.

The electronic origins of the structural trends outlined above are revealed by the compositions of the molecular orbitals of the mixed-valence system (Table 5, Figure 1b). The majority-spin t_{2g} orbitals ($6a_2$, $10b_2$, $16a_1$) on either center remain essentially localized, and the unpaired electron enters an orbital ($17a_1\uparrow$) consisting primarily of majority-spin d_{z^2} on Mn^L. The gross features of the molecular orbital diagram are therefore consistent with the presence of distinct Mn^{IV} and Mn^{III} centers. The right-hand side of the figure is very similar to one half of the symmetric $Mn_2^{IV/IV}$ dimer while the left-hand side is similar to one half of $Mn_2^{III/III}$.

Although the general features of both the geometric and electronic structure of the mixed-valence dimer can be interpreted as arising from discrete Mn^{III} and Mn^{IV} sites, a detailed analysis reveals subtle departures from this simple model. Most significantly, the HOMO of $Mn_2^{III/IV}$, $17a_1\uparrow$, is far more delocalized ($Mn^l:Mn^r = 48:12$)[38] than its counterparts in either $Mn_2^{IV/IV}$ or $Mn_2^{III/III}$. Table 5 confirms that this delocalization again involves the crossed $J_{x^2-y^2/z^2}$ pathway, and hence may be regarded as a transfer of charge from the majority-spin d_{z^2} orbital on Mn^{III} to the minority-spin $d_{x^2-y^2}$ orbital on Mn^{IV}. Although the same pathway is responsible for the delocalization of the orbitals of a_1 symmetry in all three oxidation states, its importance is clearly much greater in the mixed-valence system. The crucial role of the energetic separation of the interacting orbitals in determining the extent of delocalization has been noted above in the discussion of the orbitals of $Mn_2^{IV/IV}$. In the mixed-valence species, a combination of the greater stability and low spin polarization splitting at Mn^{IV} and the weak axial ligand field at Mn^{III} brings the vacant minority-spin $d_{x^2-y^2}$ orbital of Mn^{IV} energetically close to the occupied majority-spin d_{z^2} on Mn^{III}, favoring extensive delocalization.[38]

(38) The subtle balance of spin polarization and ligand-field splitting which determines the extent of delocalization is highly dependent on the chosen density functional. For example, if the gradient corrections are not included in the Hamiltonian, the extent of delocalization of the unpaired electron is even greater ($Mn^l:Mn^r = 43:28$), and the difference between $Mn^{III}-N^{ax}$ bond lengths in $Mn_2^{III/III}$ and $Mn_2^{III/IV}$ is increased to 0.084 Å.

(39) Calculated values of J are substantially larger if gradient corrections are neglected (−402 and −266 cm^{-1} for $Mn_2^{IV/IV}$ and $Mn_2^{III/III}$, respectively).

The population analysis in Table 6 confirms that the majority-spin t_{2g} orbitals ($d_{x^2-y^2}$, d_{xz}, d_{yz}) on both centers are fully occupied. The population of the majority-spin d_{z^2} orbital ($d_{z^2}\uparrow$) on Mn^{III}, however, is reduced from 0.99 in $Mn_2^{III/III}$ to 0.95 in the mixed-valence species, with a concomitant increase in the population of the minority-spin $d_{x^2-y^2}$ orbital ($d_{x^2-y^2}\uparrow$) on Mn^{IV} from 0.13 in $Mn_2^{IV/IV}$ to 0.25 in $Mn_2^{III/IV}$. It is important to note that even in the hypothetical limit of complete delocalization of the unpaired electron along this pathway, where both manganese centers attain an average oxidation state of +3.5, the two ions would not be electronically or geometrically equivalent—one center would have the electrons in a high-spin configuration, the other low-spin.

The delocalization of the unpaired electron along the crossed pathway between majority-spin d_{z^2} and minority-spin $d_{x^2-y^2}$ orbitals accounts for the structural features of the mixed valence species noted previously. The loss of electron density from the strongly $Mn^{III}-N^{ax}$ antibonding d_{z^2} orbital readily explains the shorter $Mn^{III}-N^{ax}$ bond compared to the symmetric $Mn_2^{III/III}$ species. The fact that the residual electron density is not transferred to the corresponding d_{z^2} orbital on the opposite center, but rather a $Mn^{IV}-N$ nonbonding $d_{x^2-y^2}$ orbital, accounts for the absence of significant structural changes at the Mn^{IV} site. Thus even in the limit of complete delocalization of the unpaired electron between the d_{z^2} and $d_{x^2-y^2}$ orbitals, significant structural asymmetry at the two Mn sites would be anticipated.

Magnetic Interactions

An analysis of the magnetic properties of dimanganese systems was recently presented by Holden Thorpe and Brudvig.[7a] A direct exchange pathway involving overlap of the $d_{x^2-y^2}$ orbitals was proposed to explain the correlation between an antiferromagnetic exchange parameter, $J/n_a n_b$ (n_a, n_b = number of electrons on each manganese center) and the exponential e^{-r} (r = Mn−Mn separation). This interpretation is not, however, consistent with the ground-state electronic structures reported above, which indicate that overlap between the orbitals in question is negligible. We are consequently forced to seek an alternative explanation for the observed magnetic data. First, we note that the data used to establish the correlation fall into three distinct classes depending on the number of oxo bridges present. A triple oxo bridge leads to short *r*Mn−Mn (2.296 Å)[40] and strong coupling, whereas a single bridge gives large *r*Mn−Mn (approximately 3.1 Å) and weak antiferromagnetic or even ferromagnetic coupling.[7] The doubly-bridged systems have intermediate Mn−Mn separations in the range of 2.7 Å and also intermediate exchange coupling parameters. Given the rather large range of Mn−Mn separations used to establish the correlation, it seems unlikely that one pathway remains dominant across the whole range. Thus while direct overlap of metal-based orbitals may be significant in the tri-μ-oxo-bridged species, it is less likely to be so at longer separations, particularly given the high oxidation states of the manganese ions. Furthermore, within the subset of di-μ-oxo-bridged species with which we are primarily concerned, the correlation between $J/n_a n_b$ and e^{-r} is far less obvious, indicating that, in this subset at least, the mechanism of magnetic exchange is more subtle.

As noted in the introductory comments, the broken-symmetry methodology has been used with some success to calculate exchange coupling constants in a variety of bimetallic systems.[23,27,28] Consequently, we were encouraged to re-examine the significant body of magnetic data available for the di-μ-oxo-bridged manganese dimers in three oxidation states. Unfortunately, the ranges of exchange coupling constants in the $Mn_2^{IV/IV}$ and $Mn_2^{III/IV}$ systems overlap to some extent, and only a single study on $Mn_2^{III/III}$ has been reported. Nevertheless, a general trend toward larger exchange coupling constants in the more highly oxidized systems is apparent from Table 1.

From the Heisenberg spin Hamiltonian

$$H = -2JS_1 \cdot S_2$$

exchange coupling constants for the symmetric species can be calculated by using an expression derived by Noodleman.[22] The energies of the broken-symmetry ground state (E_B) and the corresponding maximum spin state, S_{max}, where all metal-based electrons are aligned parallel ($S_{max} = 3$ for $Mn_2^{IV/IV}$ and 4 for $Mn_2^{III/III}$), are related by

$$E(S_{max}) - E_B = -{S_{max}}^2 J \qquad (1)$$

At the optimized geometries, calculated J values of -274 ($Mn_2^{IV/IV}$) and -172 cm^{-1} ($Mn_2^{III/III}$) were obtained by using eq 1,[39] compared to the experimental range of -140 ± 4 and -86 cm^{-1}, respectively. The overestimation of exchange coupling constants by a factor of 2 is typical of broken-symmetry density functional calculations,[23,27,41] but significantly the experimentally observed trend toward lower values of $-J$ in $Mn_2^{III/III}$ is reproduced.

For the mixed-valence species a more general spin Hamiltonian is used

$$H = -2JS_1 \cdot S_2 \pm B(S + {}^1/_2)$$

where S is the total spin quantum number and B is a resonance delocalization parameter.[41,42] The value of B may be calculated from the energies of the two delocalized high-spin states, $E(S_{max})_g$ and $E(S_{max})_u$, where the unpaired electron is placed in the symmetric and antisymmetric combinations of d_{z^2} orbitals, respectively.

$$E(S_{max})_g - E(S_{max})_u = 2B(S_{max} + {}^1/_2) \qquad (2)$$

The exchange coupling constant is then calculated by using the expression

$$E(S_{max}) - E_B = -(S_{max} + {}^1/_2)(S_{max} - {}^1/_2)J \qquad (3)$$

where the value of $E(S_{max})$ in this case is taken as the average of $E(S_{max})_g$ and $E(S_{max})_u$.

From eqs 2 and 3, we obtain values of $J = -391$ cm^{-1} and $B = 143$ cm^{-1} for $Mn_2^{III/IV}$. The value of B is significantly smaller than those calculated for other systems in the literature,[41] and also much smaller than the energy of the intervalence charge transfer band for the $Mn_2^{III/IV}$ system, ΔE_{CT} (calculated value = 13 200 cm^{-1} [$17a_1\uparrow \rightarrow 18a_1\uparrow$], experimental estimate[9] = 12 000 cm^{-1}). The mixed-valence system therefore falls clearly into the trapped category, where $B(S + {}^1/_2) << \Delta E_{CT}$, and we therefore anticipate that resonance delocalization will make a small ferromagnetic correction to J,[27,41,42] reducing its magnitude somewhat from -391 cm^{-1}. The small value of B reported above is apparently inconsistent with our proposal of significant delocalization in the mixed-valence state. The source of this apparent anomaly lies in the fact that B is calculated from the energies of the fully delocalized S_{max} states, where the crossed

(40) Wieghardt, K.; Bossek, V.; Nuber, B.; Weiss, J.; Bonvoisin, J.; Corbella, M.; Vitols, S. E.; Girerd, J.-J. *J. Am. Chem. Soc.* **1988**, *110*, 7398.

(41) Blondin, G.; Girerd, J.-J. *Chem. Rev.* **1990**, *90*, 1361.

(42) (a) Noodleman, L.; Case, D. A. *Adv. Inorg. Chem.* **1992**, *38*, 423. (b) Noodleman, L.; Baerends, E. J. *J. Am. Chem. Soc.* **1984**, *106*, 2316.

$J_{x^2-y^2/z^2}$ pathway is completely eliminated. Thus the value of 143 cm^{-1} for *B* reflects only the J_{z^2/z^2} pathway, rather than the physically more important $J_{x^2-y^2/z^2}$ pathway. We anticipate that if the true resonance delocalization could be estimated for the localized ground state, it would be larger than 143 cm^{-1}, and the magnitude of *J* would be significantly reduced from −391 cm^{-1}. In the following paragraphs, we present a simple orbital-based interpretation of the calculated magnetic properties of the manganese dimers. Given the uncertainties regarding the significance of the calculated value of *B*, and therefore in *J* for the mixed-valence species, we will focus our quantitative discussion on the two even-electron systems, $Mn_2^{IV/IV}$ and $Mn_2^{III/III}$.

In all oxidation states, both the $J_{xz/xz}$ and $J_{yz/yz}$ pathways are likely to be significant on the basis of the overlap of the metal-based orbitals with the out-of-plane oxo p_z orbitals, and consequent delocalization of the $10b_2$ and $6a_2$ orbitals over both metal centers. The $J_{x^2-y^2/x^2-y^2}$ and J_{z^2/z^2} pathways could in principal contribute if direct overlap of the metal-based orbitals occurred, but as noted above the ground-state electronic structures indicate that this is not the case. In the absence of direct overlap, the crossed $J_{x^2-y^2/z^2}$ pathway, where the orbitals are more favorably disposed for superexchange, takes on greater significance. In the $Mn_2^{IV/IV}$ dimer, the $J_{xz/xz}$ and $J_{yz/yz}$ pathways correspond to the interaction of half-filled orbitals, and therefore give rise to antiferromagnetic contributions to the overall exchange constant. In contrast, the $J_{x^2-y^2/z^2}$ pathway involves the interaction of a half-filled orbital ($d_{x^2-y^2}$) with a vacant one (d_{z^2}). In a recent paper Girerd and co-workers showed that interactions of this type give rise to small ferromagnetic contributions to the overall exchange coupling constant, thereby accounting for the observed magnetic properties of a range of μ-oxo-di-μ-acetato-bridged bimetallic systems.[43] Two-electron reduction to $Mn_2^{III/III}$ leaves the $J_{xz/xz}$ and $J_{yz/yz}$ pathways qualitatively unaltered, but now both $d_{x^2-y^2}$ and d_{z^2} are half filled, and the crossed exchange pathway gives rise to an additional antiferromagnetic contribution to the exchange coupling constant. The fact that the magnitude of the exchange coupling constant decreases upon reduction, despite the conversion of the ferromagnetic $J_{x^2-y^2/z^2}$ pathway in $Mn_2^{IV/IV}$ to an antiferromagnetic one in $Mn_2^{III/III}$, suggests that the crossed pathway does not exert a dominant influence on the magnetic properties.

An alternative explanation for the smaller magnitude of −*J* in the $Mn_2^{III/III}$ system lies in the redox-induced changes in geometry of the Mn_2O_2 core. The fully reduced species has a shorter Mn−Mn separation (2.716 Å) and less acute O−Mn−O angle (84.8°) compared to the $Mn_2^{IV/IV}$ system (2.866 Å and 77.9°, respectively). Changes in bridging architecture have been shown to play a significant role in determining the exchange coupling constants in other transition-metal-based systems.[23e,43] Accordingly, the exchange coupling constants for both the $Mn_2^{III/III}$ and $Mn_2^{IV/IV}$ systems were calculated as a function of Mn−Mn separation (Figure 3). The two geometries considered in Figure 3 (*r*Mn−Mn = 2.716 and 2.866 Å) correspond to the optimized structures of $Mn_2^{III/III}$ and $Mn_2^{IV/IV}$, respectively. The figure clearly illustrates the dominant role of the geometry of the Mn_2O_2 core in determining the exchange coupling constants. The trend toward larger values of −*J* at longer *r*Mn−Mn is common to both oxidation states and, at *r*Mn−Mn = 2.716 Å, −*J* is almost identical for $Mn_2^{IV/IV}$ and $Mn_2^{III/III}$. This observation provides further evidence that the $J_{xz/xz}$ and $J_{yz/yz}$ pathways, which are common to both systems, dominate the magnetic coupling, and that changes in the sign of the contribution from the crossed $J_{x^2-y^2/z^2}$ pathway caused by occupation of the d_{z^2} orbital are less important.

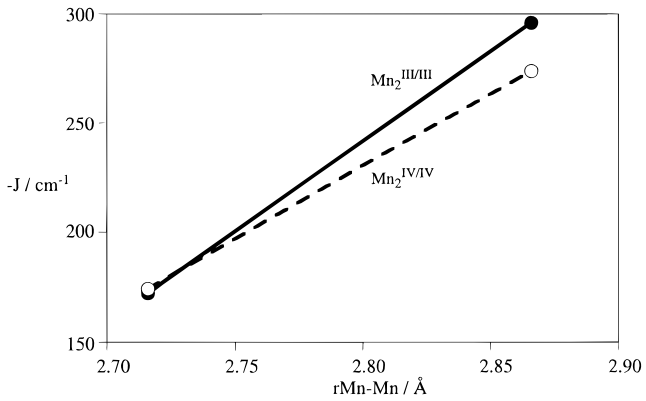

Figure 3. Dependence of calculated exchange coupling constant, −*J*, for $Mn_2^{IV/IV}$ and $Mn_2^{III/III}$ on geometry of the Mn_2O_2 core.

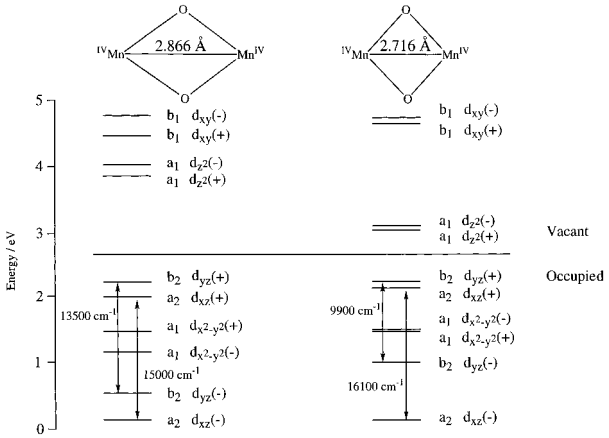

Figure 4. Dependence of the majority-spin (spin α) orbital energies for the high-spin (*S* = 3) state of $Mn_2^{IV/IV}$ on geometry of the Mn_2O_2 core.

The dependence of the $J_{xz/xz}$ and $J_{yz/yz}$ pathways on the geometry of the Mn_2O_2 core can be investigated further by considering the energies of the metal-based orbitals in the (S_{max}) states, in which all orbitals are delocalized over both metal centers. In these high spin states, the contribution of the particular exchange pathway to the ground-state *J* value is related to the energetic separation of the symmetric and antisymmetric combinations of orbitals,[28,44] and hence the relative importance of $J_{xz/xz}$ and $J_{yz/yz}$ pathways can be assessed. It is important to emphasize again that the full delocalization of the metal-based electrons in the high-spin states means that the crossed $J_{x^2-y^2/z^2}$ exchange mechanism is eliminated, and splittings between orbitals of a_1 symmetry do not contain information regarding this pathway. We reiterate, however, that trends in the overall exchange constant indicate that this pathway is of secondary importance to the dominant $J_{xz/xz}$ and $J_{yz/yz}$ mechanisms. The orbital energies shown in Figure 4 relate to the $Mn_2^{IV/IV}$ system calculated at two distinct geometries. The first corresponds to the optimized $Mn_2^{IV/IV}$ geometry (*r*Mn−Mn = 2.866 Å), while in the second the Mn_2O_2 core is compressed along the Mn−Mn axis, giving an Mn−Mn separation (2.716 Å) typical of the reduced species. This choice of systems allows us to analyze geometry-dependent changes in the exchange pathways without the added complication of changes in oxidation state. At long Mn−Mn separations, where the O−Mn−O angle is acute (78.5°), the splittings of the (+)

(43) Hotzelmann, R.; Wieghardt, K.; Flörke, U.; Haupt, H.-J.; Weatherburn, D. C.; Bonvoisin, J.; Blondin, G.; Girerd, J.-J. *J. Am. Chem. Soc.* **1992**, *114*, 1681.

(44) Hay, P. J.; Thibeault, J. C.; Hoffmann, R. *J. Am. Chem. Soc.* **1975**, *97*, 4884.

Chart 4. Dependence of the $J_{xz/xz}$ and $J_{yz/yz}$ Exchange Pathways on the O−Mn−O Angle

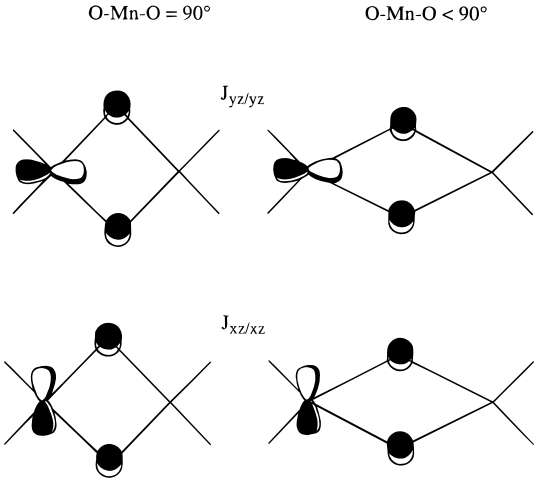

and (−) combinations of the a_2 (d_{xz}) and b_2 (d_{yz}) orbitals are 15 000 and 13 500 cm^{-1}, respectively, indicating that both $J_{xz/xz}$ and $J_{yz/yz}$ pathways contribute approximately equally to the overall ground state exchange coupling. As the Mn−Mn separation is reduced and the O−Mn−O angle approaches 90°, the splitting of the a_2 orbitals increases marginally (1100 cm^{-1}), but the b_2−b_2 separation is reduced by 3600 cm^{-1}. The geometry dependence of the overlap of metal-based d_{xz} and d_{yz} orbitals with the out-of-plane p_z orbitals on the oxo bridge is summarized in Chart 4. At the point where the O−Mn−O angle is exactly 90°, the oxo p_z orbitals overlap equally with the d_{xz} and d_{yx} orbitals. As the Mn−Mn distance increases, causing the O−Mn−O angle to narrow, the interaction with the d_{yz} (b_2) orbitals is enhanced, while that with d_{xz} (a_2) is reduced, giving rise to a smaller separation between the a_2 orbitals. The greater overlap of d_{yz} and ligand-based orbitals at long Mn−Mn separations enhances the antiferromagnetic contribution from the $J_{yz/yz}$ pathway, giving rise to the higher exchange coupling constants in the $Mn_2^{IV/IV}$ species. Identical trends emerge from a similar analysis of the $Mn_2^{III/III}$ systems, again confirming that the dominant $J_{yz/yz}$ and $J_{xz/xz}$ pathways are largely unaffected by changes in oxidation state.

In summary, the calculations indicate that the $J_{x^2-y^2/z^2}$ exchange pathway makes only minor contributions to the overall exchange coupling constant in the $Mn_2^{III/III}$ and $Mn_2^{IV/IV}$ oxidation states. Variations in J are caused principally by geometric changes which strongly influence the efficiency of the $J_{yz/yz}$ pathway. Finally, we note that the difference in Mn−Mn separations in the optimized structures of the $Mn_2^{IV/IV}$ and $Mn_2^{III/III}$ is greater than that observed in the structurally characterized analogues. Thus the experimental oxidation-state dependence of magnetic properties is likely to be less clear-cut than indicated by our theoretical analysis, and subtle structural and electronic changes induced by the different ancillary ligands may cause considerable overlap between the different oxidation states.

Concluding Remarks

In each of the bis-μ-oxo manganese systems described in this work, the metal-based electrons remain essentially localized on one center or the other, and the dimers contain discrete Mn^{IV} or Mn^{III} ions. The latter always adopt a high-spin configuration with the fourth electron in an orbital that is strongly antibonding with respect to the axial nitrogen. On the basis of favorable orientation for superexchange, we can identify three significant contributions to the metal−metal interaction. The Mn d_{xz} and d_{yz} orbitals interact *via* superexchange pathways, $J_{xz/xz}$ and $J_{yz/yz}$, mediated by the out-of-plane p_z orbitals on the oxo bridges. The third pathway, $J_{x^2-y^2/z^2}$, is mediated by a combination of in-plane oxo p_x and p_y orbitals, and links the $d_{x^2-y^2}$ orbital on one center with the torus of the d_{z^2} orbital on the opposite center. The symmetric superexchange pathways, $J_{xz/xz}$ and $J_{yz/yz}$, are found to dominate the magnetic properties of the dimers, but the "crossed" exchange pathway is highly significant in determining the electron distribution in the mixed-valence dimer.

The extent of delocalization of an electron between the $d_{x^2-y^2}$ and d_{z^2} orbitals on opposite centers is determined by the energetic separation of the single-ion orbitals, which in turn is dictated by a combination of both spin polarization and ligand-field splittings. In the symmetric $Mn_2^{IV/IV}$ and $Mn_2^{III/III}$ dimers, the energy gap is relatively large and the occupied a_1 orbitals remain essentially localized (Mn^l:Mn^r = 60:5 for $Mn_2^{IV/IV}$, 62:4 and 61:5 for $Mn_2^{III/III}$). In the mixed-valence dimer, however, a combination of the reduced ligand-field splitting in Jahn−Teller distorted Mn^{III} and the low spin polarization splitting in Mn^{IV} brings the majority-spin d_{z^2} orbital on Mn^{III} and minority-spin $d_{x^2-y^2}$ on Mn^{IV} close in energy. The result is more extensive delocalization of the unpaired electron between the two metals (48:12).[38] It is important to note that in the hypothetical limit of complete delocalization *via* this crossed $J_{x^2-y^2/z^2}$ pathway, identical manganese sites would not result. The Mn ion with electron density in the d_{z^2} orbital (Mn^{III} in the localized limit) remains in a high-spin configuration, whereas that with minority-spin $d_{x^2-y^2}$ partially occupied (Mn^{IV} in the localized limit) is low-spin. The structural data available from both crystallographic analysis and our own geometry optimizations substantiate this important distinction. In the mixed-valence $Mn_2^{III/IV}$ species, Mn^{III}−N^{ax} bonds are distinctly shorter than in the symmetric $Mn_2^{III/III}$ analogues, due to loss of electron density from the d_{z^2} orbital. In contrast, the structure of the Mn^{IV} site in the mixed valence dimers is almost identical with that in $Mn_2^{IV/IV}$, because the additional electron density enters a nonbonding $d_{x^2-y^2}$ orbital, and therefore does not significantly influence the metal−ligand bond lengths. Finally, we note that the electron paramagnetic resonance (EPR) spectrum of the oxygen-evolving complex exhibits a distinctly anisotropic metal hyperfine signal, which may be a consequence of the delocalization of electron density into the minority-spin $d_{x^2-y^2}$ orbital on Mn^{IV}, which results in a significantly anisotropic electron distribution.[45]

Acknowledgment. We express our gratitude to the Australian Research Council (ARC) for financial support.

JA964360R

(45) (a) Åhrling, K.; Pace, R. J. *Biophys. J.* **1995**, *68*, 2081. (b) Zheng, M.; Dismukes, C. *Inorg. Chem.* **1996**, *35*, 3307.